Available online at www.sciencedirect.com
ScienceDirect
Physica D 228 (2007) 140–147
PHYSICA D
www.elsevier.com/locate/physd

Boundary induced nonlinearities at small Reynolds numbers

M. Sbragaglia*, K. Sugiyama

Faculty of Applied Sciences, IMPACT, and Burgerscentrum, University of Twente, AE 7500 Enschede, The Netherlands

Received 23 November 2006; received in revised form 6 February 2007; accepted 4 March 2007
Available online 15 March 2007
Communicated by D. Lohse

Abstract

We investigate the importance of boundary slip at finite Reynolds numbers for mixed boundary conditions. Nonlinear effects are induced by the non-homogeneity of the boundary condition and change the symmetry properties of the flow with an overall mean flow reduction. To explain the observed drag modification, exact reciprocal relations in the presence of heterogeneous boundary conditions are derived. The small-Reynolds-number limit predicts a reduction of the mean flow rate from the creeping flow to be proportional to the second power of the Reynolds number. To further support our theoretical analysis, numerical simulations with the lattice Boltzmann method (LBM) and finite difference method (FDM) are performed and reveal a pronounced numerical efficiency of LBM with respect to FDM.

Keywords: Microfluidics; Laminar flows; Computational techniques; Lattice Boltzmann method

1. Introduction

The growing interest in flow properties at small scales [1,2] has recently produced new research themes and questions. In particular, the understanding of wetting behaviour, roughness effects and interfacial phenomena (see [3] for an exhaustive review) is constantly providing new perspectives on how to interpret boundary conditions for small scale hydrodynamics. A failure of the classical no-slip boundary condition is now suggested by a series of experiments [4–7] and numerical studies [8–10] for fluids confined in micro- and nano-geometries.

An appealing explanation for the observed slippage is the formation of gas pockets (bubbles) between the liquid and the solid [11] which provide sliding surfaces for the fluid and modify considerably its friction properties. For example, in recent experimental observations of fluid flows past controlled ultrahydrophobic surfaces [12,13], the authors report pressure drop reductions of the order of 40% and, in the experimental observations in [14], a significant drag reduction mechanism is believed to be induced by free slip surfaces above air-filled micro-cracks at the boundaries. In order to study the correct momentum balance in these problems one should work with the continuity and Navier–Stokes equations. Then, to provide the correct boundary conditions, the idea is to assume a no-slip boundary surface covered with some regions (strips, patches, grooves) of free slip, i.e. regions of reduced wall stress for the velocity field so as to mimic the presence of gas pockets [15–19].

When the above continuum description is involved, the first non-trivial control parameter of the flow is the Reynolds number Re. For small scale hydrodynamics, nonlinear terms are typically supposed very small (formally $Re \to 0$) but, when dealing with surface heterogeneities, it is not clear if and how they can influence the fluid by affecting Re. This is an important issue for all those experimental situations where $Re \sim \mathcal{O}(1)$ [12,14] and would be an effect with no counterpart in laminar homogeneous flows.

To clarify this point, we will consider pressure driven laminar flows with mixed boundary conditions at *finite Reynolds numbers*. To quantitatively interpret the mechanism of drag reduction, we will use reciprocal equations relating the finite Reynolds number solution to the creeping flow regime ($Re \to 0$). Scaling laws for the reduction of the mean flow rate will be obtained and all the theoretical predictions will be

* Corresponding address: Department of Physics, University of Twente, P.O. Box 217, 7500 Enschede, The Netherlands. Tel.: +31 53 489 4585; fax: +31 53 489 8068.
E-mail address: sbragaglia@roma2.infn.it (M. Sbragaglia).

0167-2789/$ - see front matter
doi:10.1016/j.physd.2007.03.004

validated in the framework of numerical simulations with the finite difference method (FDM) and lattice Boltzmann method (LBM) for mixed boundary conditions realized on strips. In this case, we identify a series of situations where the finite Reynolds number effects become important and we also provide with the LBM a new and efficient way to parametrize boundary conditions.

The paper is organized as follows: in Section 2 the physical problem is formulated mathematically and we will give the necessary background to apply finite Reynolds perturbation theory that is the subject of Section 3. In Section 4 we give a brief review of the numerical procedures used. All numerical results are discussed in Section 5 and conclusions will follow in Section 6.

2. Formulation of the problem

We will refer to a wall-bounded flow where x, z and y denote respectively the streamwise, spanwise and wall-normal coordinates. In the stationary regime, the governing equations are expressed in dimensional form as

$$\nabla^* \cdot \boldsymbol{u}^* = 0, \quad \nabla^* \cdot (\boldsymbol{u}^*\boldsymbol{u}^*) = \nabla^* \cdot \boldsymbol{\sigma}^* + \frac{1}{\rho^*}\left(-\frac{\mathrm{d}P^*}{\mathrm{d}x^*}\right)\boldsymbol{e}_x. \quad (1)$$

In the above equations, the superscript $*$ has been introduced in order to indicate dimensional quantities and to distinguish them from dimensionless ones (without superscript) to be introduced later. $\frac{\mathrm{d}P^*}{\mathrm{d}x^*}$ represents an external pressure gradient along $\boldsymbol{e}_x$ and the stress tensor $\boldsymbol{\sigma}^*$ is written as

$$\boldsymbol{\sigma}^* = -\frac{p^*}{\rho^*}\boldsymbol{I} + 2\nu^*\boldsymbol{S}^*, \quad (2)$$

with $\boldsymbol{S}^*$ the strain rate tensor and p^* the pressure. Boundary conditions on the no-slip and free slip portions of the wall (hereafter NSW and FSW) are written as

$$\boldsymbol{u}^* = 0 \quad \text{on NSW}, \quad (3)$$

$$(\boldsymbol{n} \cdot \boldsymbol{\sigma}^*) \times \boldsymbol{n} = 0 \quad \text{on FSW}, \quad (4)$$

where $\boldsymbol{n}$ is the wall-normal unit vector. Since we are interested in local and global effects on the flow, we use periodicity boundary conditions in the streamwise and spanwise directions which is also consistent with the available experimental and numerical works [9,12,13]. Two walls are then considered at $y = 0$ and $y = L_y$ and we will refer to the slip percentage, ξ, as the ratio between the free slip area and the total one. To proceed further, let us consider the friction velocity u_τ and the *friction Reynolds number* Re_τ defined as

$$u_\tau = \sqrt{\tau_w} \qquad Re_\tau = \frac{u_\tau(L_y/2)}{\nu} \quad (5)$$

where τ_w is the skin friction averaged over the wall surface. If we impose the same boundary conditions on $y = 0$ and $y = L_y$ (see also Fig. 1), we obtain the relation between the skin friction and the driving pressure gradient:

$$\tau_w = \nu\left\langle\frac{\partial u}{\partial y}\right\rangle_{y=0} = -\nu\left\langle\frac{\partial u}{\partial y}\right\rangle_{y=L_y} = \frac{L_y}{2\rho}\left(-\frac{\mathrm{d}P}{\mathrm{d}x}\right) \quad (6)$$

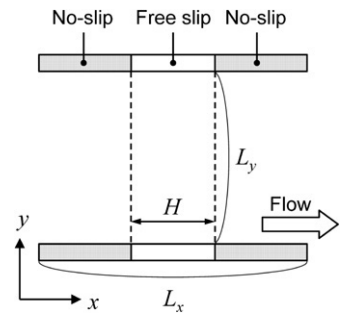

Fig. 1. A sketch of the channel used for numerical simulations. We use a $2d$ channel with the same boundary conditions on the top and bottom walls. Free slip conditions are imposed on a width H on both walls giving a slip percentage $\xi = H/L_x$. We also impose periodicity boundary conditions in the streamwise (x) direction.

where $\langle\cdot\rangle$ represents the volume average operator. This immediately implies

$$Re \propto Re_\tau^2 \quad (7)$$

where Re is the *bulk Reynolds number* defined as $Re = \left(-\frac{\mathrm{d}P}{\mathrm{d}x}\right)\frac{L_y^3}{8\rho\nu^2}$. Now, we choose u_τ and $L_y/2$ as the velocity and length scales for normalization. This means that the two walls are located at $y = 0$ and $y = 2$ and that the velocity components and the pressure fields satisfy the following dimensionless equations:

$$\nabla \cdot \boldsymbol{u} = 0, \qquad \nabla \cdot (\boldsymbol{u}\boldsymbol{u}) = \nabla \cdot \boldsymbol{\sigma} + \boldsymbol{e}_x \quad (8)$$

with the boundary conditions

$$\boldsymbol{u} = 0 \quad \text{on NSW}, \quad (9)$$

$$(\boldsymbol{n} \cdot \boldsymbol{\sigma}) \times \boldsymbol{n} = 0 \quad \text{on FSW}, \quad (10)$$

where the pressure has been normalized with the term $(\rho^* u_\tau^2)$ and the dimensionless stress tensor is given by

$$\boldsymbol{\sigma} = -p\boldsymbol{I} + \frac{2}{Re_\tau}\boldsymbol{S}.$$

We also introduce the velocity vector $\tilde{\boldsymbol{u}}$ and the pressure $\tilde{p}$ satisfying the following equations for the creeping flow with no advection:

$$\nabla \cdot \tilde{\boldsymbol{u}} = 0, \qquad \nabla \cdot \tilde{\boldsymbol{\sigma}} + \boldsymbol{e}_x = 0, \quad (11)$$

with the boundary conditions

$$\tilde{\boldsymbol{u}} = 0 \quad \text{on NSW}, \quad (12)$$

$$(\boldsymbol{n} \cdot \tilde{\boldsymbol{\sigma}}) \times \boldsymbol{n} = 0 \quad \text{on FSW}. \quad (13)$$

In this case, $\tilde{\boldsymbol{u}}$, $\tilde{\boldsymbol{\sigma}}$ and $\tilde{p}$ represent the zeroth order approximation for the velocity field, stress tensor and pressure field and they will be used to quantify the effects of a finite Reynolds number. Our starting point is the application of reciprocal relations [20] to the fields $\boldsymbol{u}$ and $\tilde{\boldsymbol{u}}$ and their stresses. In fact it can be shown that

$$(\nabla\boldsymbol{u}):\tilde{\boldsymbol{\sigma}} = (\nabla\tilde{\boldsymbol{u}}):\boldsymbol{\sigma} \quad (14)$$

is an exact relation between the above fields. Since $\boldsymbol{n}\cdot\tilde{\boldsymbol{\sigma}}\cdot\boldsymbol{u}=0$ on the wall, taking the volume integral of the lhs of (14) over the whole fluid region, we obtain

$$\begin{aligned}\int_{\text{fluid}} \mathrm{d}^3\boldsymbol{x}(\nabla\boldsymbol{u}):\tilde{\boldsymbol{\sigma}} &= -\int_{\text{fluid}} \mathrm{d}^3\boldsymbol{x}\boldsymbol{u}\cdot(\nabla\cdot\tilde{\boldsymbol{\sigma}}) \\ &\quad + \int_{\text{fluid}} \mathrm{d}^3\boldsymbol{x}\nabla\cdot(\boldsymbol{u}\cdot\tilde{\boldsymbol{\sigma}}) \\ &= \int_{\text{fluid}} \mathrm{d}^3\boldsymbol{x}\boldsymbol{u}\cdot\boldsymbol{e}_x + \oint_{\text{wall}} \mathrm{d}^2\boldsymbol{x}\,\boldsymbol{n}\cdot\tilde{\boldsymbol{\sigma}}\cdot\boldsymbol{u} \\ &= L_xL_yL_z\langle u\rangle. \end{aligned} \tag{15}$$

In a similar way, for the rhs of (14), we obtain

$$\begin{aligned}\int_{\text{fluid}} \mathrm{d}^3\boldsymbol{x}(\nabla\tilde{\boldsymbol{u}}):\boldsymbol{\sigma} &= \int_{\text{fluid}} \mathrm{d}^3\boldsymbol{x}\tilde{\boldsymbol{u}}\cdot\boldsymbol{e}_x - \int_{\text{fluid}} \mathrm{d}^3\boldsymbol{x}\tilde{\boldsymbol{u}}\cdot\{(\boldsymbol{u}\cdot\nabla)\boldsymbol{u}\} \\ &\quad + \oint_{\text{wall}} \mathrm{d}^2\boldsymbol{x}\boldsymbol{n}\cdot\boldsymbol{\sigma}\cdot\tilde{\boldsymbol{u}} \\ &= L_xL_yL_z\langle\tilde{u}\rangle - \int_{\text{fluid}} \mathrm{d}^3\boldsymbol{x}\tilde{\boldsymbol{u}}\cdot\{(\boldsymbol{u}\cdot\nabla)\boldsymbol{u}\} \end{aligned} \tag{16}$$

where the second term in the rhs is

$$\begin{aligned}-\int_{\text{fluid}} \mathrm{d}^3\boldsymbol{x}\tilde{\boldsymbol{u}}\cdot\{(\boldsymbol{u}\cdot\nabla)\boldsymbol{u}\} &= \int_{\text{fluid}} \mathrm{d}^3\boldsymbol{x}\nabla\cdot\{\boldsymbol{u}(\boldsymbol{u}\cdot\tilde{\boldsymbol{u}})\} \\ &\quad + \int_{\text{fluid}} \mathrm{d}^3\boldsymbol{x}(\boldsymbol{u}\boldsymbol{u}):(\nabla\tilde{\boldsymbol{u}}) \\ &= \oint_{\text{wall}} \mathrm{d}^2\boldsymbol{x}\boldsymbol{n}\cdot\{\boldsymbol{u}(\boldsymbol{u}\cdot\tilde{\boldsymbol{u}})\} \\ &\quad + L_xL_yL_z\langle(\boldsymbol{u}\boldsymbol{u}):(\nabla\tilde{\boldsymbol{u}})\rangle. \end{aligned} \tag{17}$$

Using (15)–(17) and the fact that $\boldsymbol{n}\cdot\boldsymbol{u}=0$ on the wall, we obtain the contribution of advection to the change of the flow rate

$$\langle u\rangle - \langle\tilde{u}\rangle = \langle(\boldsymbol{u}\boldsymbol{u}):(\nabla\tilde{\boldsymbol{u}})\rangle. \tag{18}$$

Expression (18) exactly decouples the effect of Stokes flow from the advection and it applies for every Reynolds number and every realization of the boundary conditions. It is an exact expression for any periodic flow and it will help us to interpret the quantitative mechanism of the velocity deficit with respect to the Stokes flow solution. It is also important that, if we apply no-slip boundary conditions, expression (18) is equivalent to the identity of the Reynolds shear stress contribution to the friction coefficient in a flow bounded with no-slip walls derived in [21]. But, since (18) is written in a more general form, it can be used to extensively characterize skin friction problems with heterogeneous boundary conditions. In particular we will show how it is possible to derive scaling law relations from (18) for small Reynolds number and with the use of numerical simulations we will further investigate its validity for higher Reynolds numbers where the regular perturbation is no longer valid.

3. Finite Re_τ perturbation theory

Using the perturbation method with respect to the friction Reynolds number Re_τ, the effect of the advection on the change of the flow rate $\langle u\rangle - \langle\tilde{u}\rangle$ is now examined. More precisely, we do not directly solve the perturbation equation but we want to consider the following relation

$$\langle u\rangle/\langle\tilde{u}\rangle - 1 = \Gamma Re_\tau^n$$

(here Γ is a coefficient) for small Re_τ and concentrate on the exponent n. In our present approach, $\boldsymbol{u}$ and p in (8) are regularly expanded with respect to Re_τ in the following form

$$\boldsymbol{u} = Re_\tau^1\boldsymbol{u}^{(0)} + Re_\tau^3\boldsymbol{u}^{(1)} + Re_\tau^5\boldsymbol{u}^{(2)} + \cdots, \tag{19}$$

$$p = Re_\tau^0 p^{(0)} + Re_\tau^2 p^{(1)} + Re_\tau^4 p^{(2)} + \cdots, \tag{20}$$

where the superscript (0) indicates the creeping flow solution,

$$\tilde{\boldsymbol{u}} = Re_\tau\boldsymbol{u}^{(0)}, \qquad \tilde{p} = p^{(0)}. \tag{21}$$

Note that the even order (i.e., $O(Re_\tau^{2n})$) components of the velocity vector are identically zero because there is no advection or forcing to balance the divergence of the stress tensor containing the $O(Re_\tau^{2n})$ velocity. The arguments given in Appendix show that

$$\langle u\rangle/\langle\tilde{u}\rangle - 1 = \Gamma Re_\tau^4,$$

with the prefactor

$$\Gamma = \left\langle \boldsymbol{u}^{(1)}\cdot\left\{(\boldsymbol{u}^{(0)}\cdot\nabla)\boldsymbol{u}^{(0)}\right\}\right\rangle \Big/ \langle u^{(0)}\rangle$$

which is dependent upon the perturbed velocity component but independent of the Reynolds number. Alternatively, if one is interested in a scaling relation with respect to the bulk Reynolds number, it follows immediately from (7) that

$$\langle u\rangle/\langle\tilde{u}\rangle - 1 \sim Re^2. \tag{22}$$

This effect is physically induced by the boundary condition ($\Gamma \neq 0$) and it develops with very well defined scaling laws with respect to the Reynolds number. If the flow rate is fixed, the total dissipation rate is proportional to the driving pressure gradient, which equals the skin friction divided by the channel half width. This means that the deviation of the velocity from the creeping flow due to advection enhances the total skin friction. It can be thus interpreted that a larger driving force than in creeping flow is required at finite Reynolds numbers to maintain a given flow rate. Equivalently, with fixed driving pressure gradient and viscosity, the flow rate should decrease due to advection. For these reasons, a decrease of the averaged mass flow rate for a fixed pressure drop is expected and we derive the exact scaling law that drives this change for small Reynolds numbers. Now, in order to validate this picture and also to study the problem in the region where the regular perturbation theory is no longer valid, we will make use of numerical simulations for mixed boundary conditions realized on strips.

4. Numerical procedures

The numerical techniques used are finite difference method (FDM) and lattice Boltzmann method (LBM). Both methods

will be compared under the same set of physical parameters and, independently of the present computational details, the general conclusions drawn in the paper will not be spoiled if studied in the context of other numerical procedures.

In the FDM, the equations are discretized in an Eulerian framework on a staggered grid [22]. A second-order scheme, i.e. the Adams–Bashforth method for the advection term and the Crank–Nicolson one for the viscous term, is used to integrate the equations in time [23]. The pressure is treated implicitly. The space derivatives are approximated by the fourth-order central difference scheme. For the advection term, we employ the scheme by Kajishima et al. in [24].

In solving the Poisson equation, we use the Fast Fourier Transform (FFT) for high speed and accuracy. The three-dimensionally discretized equations are then reduced to a one-dimensional problem by taking the FFT in the streamwise and spanwise directions. The reduced-order equation written in the heptadiagonal matrix form is directly solved. Since we use a staggered grid system, the velocity parallel to the wall is not located on the wall. In order to approximate the boundary conditions on the wall, the velocity at a virtual point outside the flow region is adjusted using the third-order Lagrange extrapolation.

The other numerical technique used is a mesoscopic approach based on the Boltzmann equations and known as lattice Boltzmann method (LBM) [25–27]. This method is a kinetic approach to fluid flows that starts from the Boltzmann equation discretized over a time lapse Δt

$$f_i(\boldsymbol{x}+\boldsymbol{c}_i\Delta t, t+\Delta t) - f_i(\boldsymbol{x}, t) = -\frac{\Delta t}{\tau}(f_i(\boldsymbol{x}, t) - f_i^{(eq)}(\boldsymbol{x}, t)) + F_i. \tag{23}$$

The left hand side represents a streaming term for a probability density function ($f_i(\boldsymbol{x}, t)$) to find in a given position and time $(\boldsymbol{x}, t)$ a kinetic particle whose velocity is $\boldsymbol{c}_i$. Here the set of velocities is properly discretized ($i = 0 \ldots N$). The right hand side represents a simplified version of the standard collision term in the real Boltzmann equation: it expresses a relaxation (with characteristic time τ) towards a local equilibrium ($f_i^{(eq)}$), the equivalent of the local Maxwellian equilibrium in kinetic theory [28]. Finally the term F_i is an external volume forcing used to produce a constant pressure drop ($\mathrm{d}P/\mathrm{d}x$) in the streamwise direction. Starting from the kinetic Eq. (23) and coarse-graining (in the velocity space) the kinetic distributions, one obtains respectively a macroscopic density and velocity field as follows:

$$\rho(\boldsymbol{x}, t) = \sum_{i=0}^{N} f_i(\boldsymbol{x}, t) \qquad \boldsymbol{u}(\boldsymbol{x}, t) = \frac{1}{\rho(\boldsymbol{x}, t)}\sum_{i=0}^{N} \boldsymbol{c}_i f_i(\boldsymbol{x}, t). \tag{24}$$

Then, using the Chapman–Enskog expansions (see [26] for all the details), one can show that the macroscopic fields (24) satisfy the continuity and momentum equations of fluid mechanics. In principle, the convergence of LBM to Navier–Stokes equations might fail to be reached as the Reynolds number becomes smaller and smaller. As it will be shown in the numerics, this does not affect and spoil the final result allowing a quantitative agreement between LBM and FDM. Concerning the subject of boundary conditions for LBM, various approaches have been proposed [29–32]. The simplest application to introduce slip at the boundaries involves a *slip function*, $s(\boldsymbol{x})$, representing the probability for a particle to slip (conversely, $1 - s(\boldsymbol{x})$ will correspond to the probability for the particle to be bounced back) [32]. The emerging macroscopic boundary condition for the velocity field can be written as

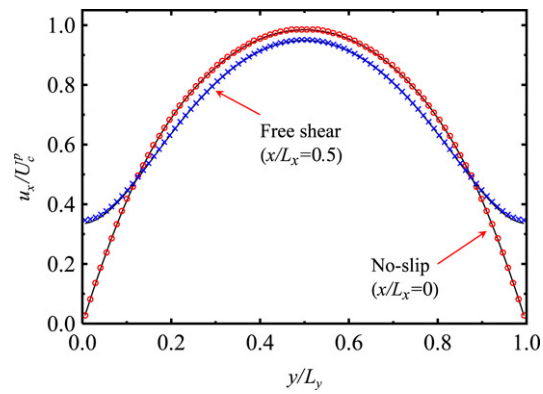

Fig. 2. Velocity profiles along a channel with mixed boundary conditions of free slip and no-slip. In the inlet region (○ for LBM and lines for FDM), due to the no-slip condition the profile is almost a parabolic one with zero velocity at the boundaries and constant concavity. In the middle of the channel (× for LBM and lines for FDM), the free slip condition produces an enhancement of the local slip properties at the boundaries with a reduction of the profiles in the bulk region. In both cases all the profiles are normalized with respect to the center channel velocity in the Poiseuille limit.

$$\boldsymbol{u}_{\parallel}(\boldsymbol{x}) \sim \frac{s(\boldsymbol{x})}{1 - s(\boldsymbol{x})}\partial_n \boldsymbol{u}_{\parallel}(\boldsymbol{x}) \tag{25}$$

where $\boldsymbol{u}_{\parallel}$ represents the tangential velocity field at a solid surface. In this language, the usual no-slip boundary conditions are recovered in the limit $s(\boldsymbol{x}) \to 0$, while the perfect free slip profile is obtained with $s(\boldsymbol{x}) \to 1$.

5. Numerical results

For the numerical results we concentrate on the case of transversal strips. We carry out numerical simulations in a two-dimensional channel with dimensions L_x (stream wise) and L_y (wall-normal). The boundary condition of free slip is concentrated in a segment H on both top and bottom walls with a slip percentage ξ given by $\xi = H/L_x$ (see Fig. 1).

In Fig. 2 we show the velocity profiles along the channel for the case with $Re_\tau = 2.245$. In the inlet region the profile is of Poiseuille type (parabolic profile with zero slip) while in the middle of the slip region the local stress at the boundaries is zero and consequently the local viscous stress is minimized.

In order to quantify the slip effects, we use the slip length l_s directly evaluated from the mass flow rate Q_{eff}:

$$Q_{\mathrm{eff}} = \int_0^{L_y} u_x \mathrm{d}y = Q_{\mathrm{pois}}\left(1 + 6\frac{l_s}{L_y}\right) \tag{26}$$

where Q_{pois} is the mass flow rate in the Poiseuille limit $Q_{\mathrm{pois}} = \frac{1}{12\rho\nu}\left(-\frac{\mathrm{d}P}{\mathrm{d}x}\right)L_y^3$. In Fig. 3 the slip length is shown as a function

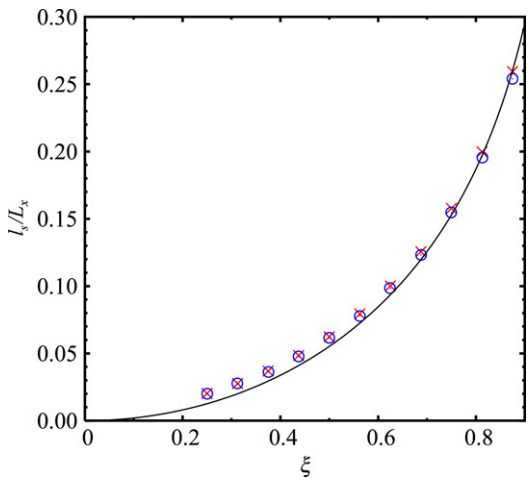

Fig. 3. Slip length normalized to the pattern dimension as a function of the slip percentage ξ. We show the results for LBM (∘) and FDM (×). Both numerical schemes are compared with the analytical estimate (line) given in [15]. The numerical simulations are carried out with the following set of parameters: $Re_\tau = 2.245$, $\rho = 1$, $L_x = 64$, $L_y = 84$, $\nu = 1/6$, $-\mathrm{d}P/\mathrm{d}x = 1.889 \times 10^{-6}$.

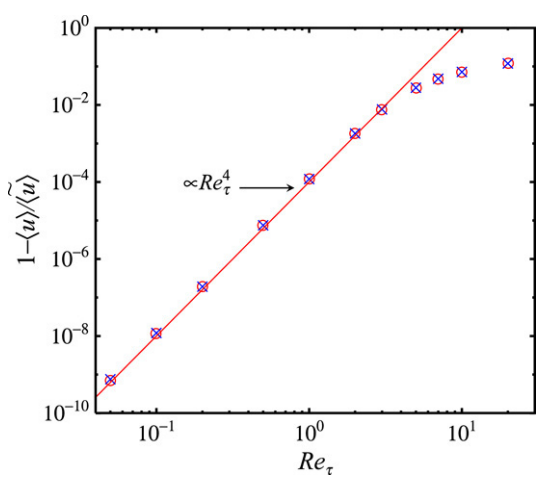

Fig. 4. Drag modification at finite Reynolds numbers. We show the relative departure from the creeping flow solution, $1 - \langle u\rangle/\langle\tilde{u}\rangle$ (∘), as a function of the friction Reynolds number Re_τ. To verify the correctness of relation (27) we also plot the right hand side of this relation (×). All the results have been obtained with FDM with numerical grid mesh $L_x = 64$, $L_y = 64$ and parameters $\rho = 1$, $\nu = 1/6$, $\xi = 0.5$. The pressure gradient $\mathrm{d}P/\mathrm{d}x$ has been changed to vary Re_τ. To emphasize the scaling behavior with respect to Re_τ, the power law Re_τ^4 is also plotted.

of ξ for a friction Reynolds number $Re_\tau = 2.245$. The slip length has been obtained from steady state configurations with FDM and LBM and results are also compared with the analytical estimate given in [15] for pressure driven Stokes flows coupled to mixed boundary conditions of no-slip and free slip realized on strips. In this case small discrepancies are observed due to a finite value of the Reynolds number.

Fig. 4 shows the relative departure from the creeping flow solution $1 - \langle u\rangle/\langle\tilde{u}\rangle$ for various friction Reynolds numbers. When increasing Re_τ, $\langle u\rangle/\langle\tilde{u}\rangle$ decreases due to the advection. With a homogeneous no-slip condition at the wall, $\langle u\rangle/\langle\tilde{u}\rangle$ would be independent of Re_τ. On the other hand, when the mixed boundary condition (as in this case) is switched on,

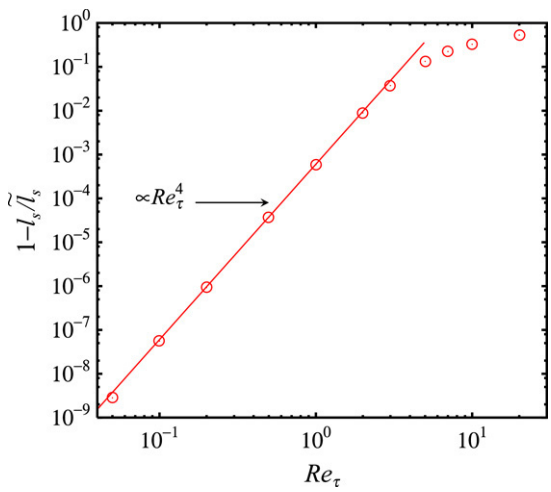

Fig. 5. Slip length at finite Reynolds numbers. We show the slip length normalized to the creeping flow counterpart, as a function of the friction Reynolds number Re_τ. All the results have been obtained with FDM with numerical grid mesh $L_x = 64$, $L_y = 64$ and parameters $\rho = 1$, $\nu = 1/6$, $\xi = 0.5$. The pressure gradient $\mathrm{d}P/\mathrm{d}x$ has been changed to vary Re_τ. In order to highlight the scaling behavior with respect to Re_τ, the power law behavior Re_τ^4 is also represented. Note that for $Re_\tau \sim 10$, the overall slip length differs from its creeping flow counterpart of the order of 10%.

$\langle u\rangle/\langle\tilde{u}\rangle$ shows a dependency on Re_τ, even in the laminar regime under consideration. According to the prediction of Section 3, the drag modification is proportional to the fourth power of the friction Reynolds number and this can be verified explicitly from this plot. More precisely, relation (18) would imply

$$1 - \langle u\rangle/\langle\tilde{u}\rangle = -\langle(\boldsymbol{uu}):(\nabla\tilde{\boldsymbol{u}})\rangle/\langle\tilde{u}\rangle \tag{27}$$

and to verify the correctness of this relation, together with $1 - \langle u\rangle/\langle\tilde{u}\rangle$ we plot also the right hand side of (27) and we observe an excellent agreement between the two contributions.

In Fig. 5, for the same set of parameters as Fig. 4, we show the relative change of the slip length with respect to the creeping flow solution. As expected, the same scaling behavior is observed and finite Reynolds effects become of the order of 10% soon after the friction Reynolds number is $Re_\tau \sim 10$.

In Figs. 6 and 7 the streamwise velocity along the channel is shown for two friction Reynolds numbers $Re_\tau = 2.245$ and $Re_\tau = 10.04$. For the smallest $Re_\tau = 2.245$ the profile is almost symmetric around the slip area but when Re_τ is increased, an asymmetry develops due to advection. This asymmetry is responsible for the drag modification observed in the simulations and it develops as a function of the Reynolds number. As one can see, for a drag enhancement of 10% the degree of asymmetry of the streamwise profile is of the same order.

In Fig. 8, the relative change $1 - \langle u\rangle/\langle\tilde{u}\rangle$ is considered for $\xi = 0.25$, $\xi = 0.5$ and $\xi = 0.75$. Using both LBM and FDM, excellent agreement is observed with respect to the functional behavior $\sim Re_\tau^4$ down to relative changes of 10^{-8}. This is a stringent benchmark test of the degree of accuracy of both numerical procedures.

Finally, in Fig. 9 the value of Γ, as extracted from the numerical simulations, is shown as a function of ξ. As ξ approaches 1 the value of Γ is higher due to the fact that

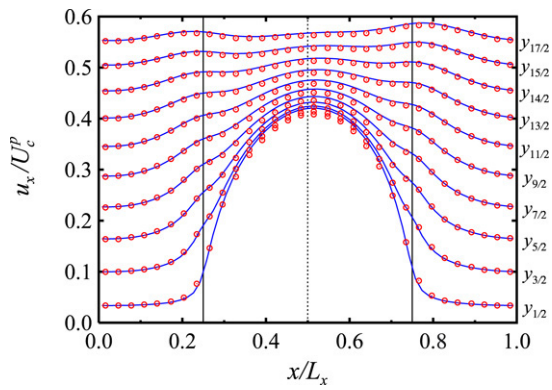

Fig. 6. Streamwise profiles for small Reynolds number. We plot the streamwise profiles as a function of the relative position along the channel for different distances from the wall ($y_{n+\frac{1}{2}}$ with $n = 0, 1, 2, \ldots$ and the wall located at $y_0 = 0$). Here we show a case with friction Reynolds number $Re_\tau = 2.245$ and parameters $\rho = 1$, $L_x = 64$, $L_y = 84$, $\nu = 1/6$, $-\mathrm{d}P/\mathrm{d}x = 1.889 \times 10^{-6}$, $\xi = 0.5$. The velocity is normalized with respect to the center channel velocity of the corresponding Poiseuille profile and both LBM (○) and FDM (lines) indicate an almost symmetric configuration with respect to the axis of the slip area (see dotted line). This is predicted by the symmetry properties of the Stokes solution ($Re_\tau \to 0$) and it is here expected to hold with very small corrections due to the finite Reynolds effects.

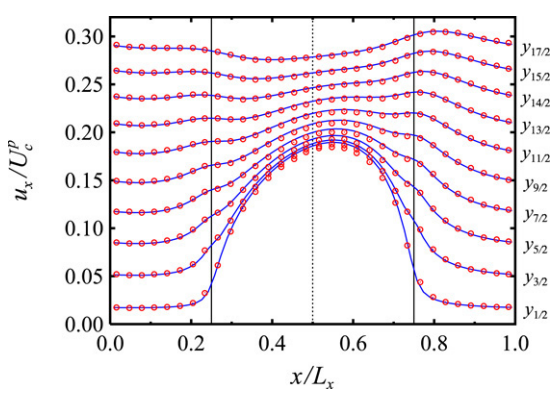

Fig. 7. Same as Fig. 6 with the following set of parameters: $Re_\tau = 10.04$ and $\rho = 1$, $L_x = 64$, $L_y = 168$, $\nu = 1/6$, $-\mathrm{d}P/\mathrm{d}x = 4.72 \times 10^{-6}$, $\xi = 0.5$. Now, due to the increase of the Reynolds number the profile becomes more asymmetric with respect to the case of Fig. 6. To highlight this effect we plot the symmetry axis of the free slip strip to be compared with the symmetry properties of the flow.

the effect of the nonlinear terms is enhanced and non-trivially triggered by the boundary condition.

6. Conclusions

The effective slip properties of flows subject to mixed-slip boundary conditions have been studied as functions of the boundary geometry and Reynolds number (Re). We have derived the exact stationary relation

$$\langle u \rangle - \langle \tilde{u} \rangle = \langle (\boldsymbol{u}\boldsymbol{u}) : (\nabla \tilde{\boldsymbol{u}}) \rangle \tag{28}$$

which can be used to characterize problems with heterogeneous boundary conditions. We have shown how to use relation (28) to interpret the quantitative mechanism for drag enhancement of the velocity field ($\boldsymbol{u}$) from its creeping flow counterpart ($\tilde{\boldsymbol{u}}$).

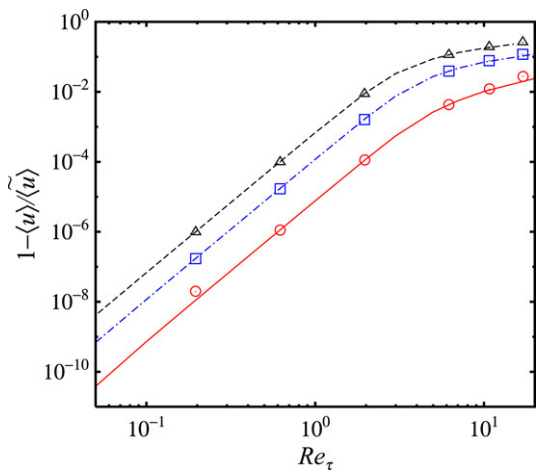

Fig. 8. Drag modification and its scaling behavior with respect to the friction Reynolds number for different values of the slip percentage ξ. We show the relative departure from the creeping flow solution, $1 - \langle u \rangle / \langle \tilde{u} \rangle$ estimated with LBM (circles for $\xi = 0.25$, squares for $\xi = 0.5$ and diamonds for $\xi = 0.75$) and FDM (solid, dotted lines). All the results have been obtained with parameters $\rho = 1$, $L_x = 64$, $L_y = 64$, $\nu = 1/6$, $\xi = 0.5$. The pressure gradient $\mathrm{d}P/\mathrm{d}x$ has then been changed to vary Re_τ. In the small Re_τ regime it is observed that the scaling relation is proportional to Re_τ^4 predicted by our analytical analysis.

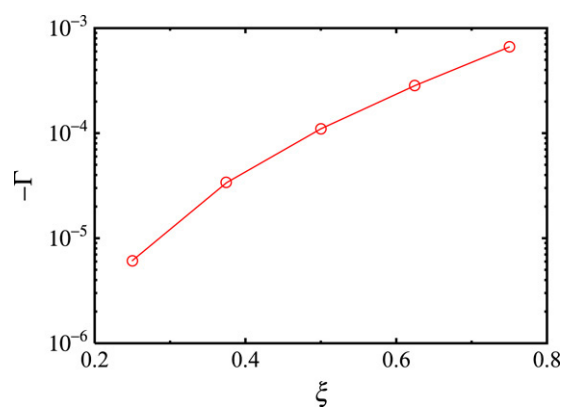

Fig. 9. The value of $-\Gamma$ as defined by the relation $\langle u \rangle / \langle \tilde{u} \rangle - 1 = \Gamma Re_\tau^4$ is shown for different values of ξ.

The physical idea underlying this behaviour is connected to the introduction of advection: at the borderline between no-slip and free slip regions, small velocity contributions close to no-slip walls are advected into the region just above the free slip boundary. This reduces the velocity field in the free slip region with an overall effect in the mass flow rate. In particular, we find that this drag modification develops from the creeping flow with a scaling law behaviour in the bulk Reynolds number as $\sim Re^2$.

To support our theoretical analysis we have carried out numerical simulations with finite difference method (FDM) and lattice Boltzmann method (LBM) and mixed boundary conditions of no-slip and free slip realized on strips. For small Reynolds numbers the predicted scaling relation is well verified by the numerical computations up to $Re \sim 1$ while the corresponding laminar flow field loses its symmetry properties in the channel, with macroscopic effects up to 10% in the effective slip length.

Relation (28) is here applied to heterogeneous slip conditions but its range of applicability is broader due to the fact that it is an exact relation for any periodic flow bounded by walls having heterogeneous boundary conditions at any Reynolds number. One would then be able to apply it also to situations with higher Reynolds numbers and not only with mixed slip boundary conditions but also with rough surfaces.

From the numerical point of view, the use of LBM has also revealed a pronounced efficiency with respect to FDM and is an optimal candidate to model with flexibility boundary conditions in hydrodynamical systems, something that is important for a cooperative relationship between experiments and theory.

Acknowledgments

We acknowledge Prof. D. Lohse and Prof. A. Prosperetti for constructive discussions and a critical reading of the manuscript.

Appendix

In this appendix we will detail the calculation leading to the analytical expressions used throughout the text. Let us assume $0 < Re_\tau \ll 1$ and expand $\boldsymbol{u}$ and p with respect to Re_τ in the following form

$$\boldsymbol{u} = Re_\tau^1 \boldsymbol{u}^{(0)} + Re_\tau^3 \boldsymbol{u}^{(1)} + Re_\tau^5 \boldsymbol{u}^{(2)} + \cdots, \tag{29}$$

$$p = Re_\tau^0 p^{(0)} + Re_\tau^2 p^{(1)} + Re_\tau^4 p^{(2)} + \cdots, \tag{30}$$

where the superscript (0), indicate the creeping flow solution,

$$\tilde{\boldsymbol{u}} = Re_\tau \boldsymbol{u}^{(0)}, \qquad \tilde{p} = p^{(0)}. \tag{31}$$

All the even orders (i.e., $O(Re_\tau^{2n})$) of the velocity vector are identically zero because there is not any advection or driving forcing to balance with the divergence of the stress tensor containing the $O(Re_\tau^{2n})$ velocity.

The continuity equation is now expressed as

$$\nabla \cdot \boldsymbol{u}^{(n)} = 0 \quad (n = 0, 1, \ldots). \tag{32}$$

The $O(Re_\tau^0)$, $O(Re_\tau^2)$ and $O(Re_\tau^4)$ momentum equations are respectively written as

$$0 = -\nabla p^{(0)} + \nabla^2 \boldsymbol{u}^{(0)} + \boldsymbol{e}_x,$$
$$\nabla \cdot (\boldsymbol{u}^{(0)}\boldsymbol{u}^{(0)}) = -\nabla p^{(1)} + \nabla^2 \boldsymbol{u}^{(1)},$$
$$\nabla \cdot (\boldsymbol{u}^{(1)}\boldsymbol{u}^{(0)} + \boldsymbol{u}^{(0)}\boldsymbol{u}^{(1)}) = -\nabla p^{(2)} + \nabla^2 \boldsymbol{u}^{(2)}.$$

For $n = 0$, 1 and 2, the boundary conditions are given by

$$\boldsymbol{u}^{(n)} = 0 \quad \text{on NSW},$$
$$(\boldsymbol{n} \cdot \boldsymbol{S}^{(n)}) \times \boldsymbol{n} = 0 \quad \text{on FSW},$$

where $\boldsymbol{S}^{(n)} = \frac{1}{2}\left\{\nabla \boldsymbol{u}^{(n)} + (\nabla \boldsymbol{u}^{(n)})^T\right\}$. With these expansions, starting from Eq. (18), we obtain the following relation

$$\begin{aligned}\langle u \rangle - \langle \tilde{u} \rangle &= Re_\tau^3 \langle u^{(1)} \rangle + Re_\tau^5 \langle u^{(2)} \rangle \\ &= Re_\tau^3 \langle (\boldsymbol{u}^{(0)}\boldsymbol{u}^{(0)}) : (\nabla \boldsymbol{u}^{(0)}) \rangle \\ &\quad + Re_\tau^5 \langle (\boldsymbol{u}^{(1)}\boldsymbol{u}^{(0)}) : (\nabla \boldsymbol{u}^{(0)}) \rangle \\ &\quad + Re_\tau^5 \langle (\boldsymbol{u}^{(0)}\boldsymbol{u}^{(1)}) : (\nabla \boldsymbol{u}^{(0)}) \rangle.\end{aligned} \tag{33}$$

The first and second terms in the rhs of Eq. (33) are zero because the kernel of the volume integral is written in the divergence form which can be rewritten using the area integral with no wall-normal flux:

$$\begin{aligned}&\int_{\text{fluid}} \mathrm{d}^3\boldsymbol{x} (\boldsymbol{u}^{(0)}\boldsymbol{u}^{(0)}) : (\nabla \boldsymbol{u}^{(0)}) \\ &= \int_{\text{fluid}} \mathrm{d}^3\boldsymbol{x} \nabla \cdot \left\{\boldsymbol{u}^{(0)} (\boldsymbol{u}^{(0)} \cdot \boldsymbol{u}^{(0)})/2\right\} \\ &= \oint_{\text{wall}} \mathrm{d}^2\boldsymbol{x} (\boldsymbol{n} \cdot \boldsymbol{u}^{(0)})(\boldsymbol{u}^{(0)} \cdot \boldsymbol{u}^{(0)})/2 = 0,\end{aligned} \tag{34}$$

$$\begin{aligned}&\int_{\text{fluid}} \mathrm{d}^3\boldsymbol{x} (\boldsymbol{u}^{(1)}\boldsymbol{u}^{(0)}) : (\nabla \boldsymbol{u}^{(0)}) \\ &= \int_{\text{fluid}} \mathrm{d}^3\boldsymbol{x} \nabla \cdot \left\{\boldsymbol{u}^{(1)} (\boldsymbol{u}^{(0)} \cdot \boldsymbol{u}^{(0)})/2\right\} \\ &= \oint_{\text{wall}} \mathrm{d}^2\boldsymbol{x} (\boldsymbol{n} \cdot \boldsymbol{u}^{(1)})(\boldsymbol{u}^{(0)} \cdot \boldsymbol{u}^{(0)})/2 = 0.\end{aligned} \tag{35}$$

The third term in the rhs of (33) is the only one that can take a non-zero value. Therefore, we obtain

$$\langle u \rangle - \langle \tilde{u} \rangle \to Re_\tau^5 \left\langle \boldsymbol{u}^{(1)} \cdot \left\{(\boldsymbol{u}^{(0)} \cdot \nabla)\boldsymbol{u}^{(0)}\right\}\right\rangle \quad \text{as } Re_\tau \to +0. \tag{36}$$

We also note that $\langle \tilde{u} \rangle = Re_\tau \langle u^{(0)} \rangle$ and so

$$\langle u \rangle / \langle \tilde{u} \rangle - 1 = \Gamma Re_\tau^4,$$

with the prefactor

$$\Gamma = \left\langle \boldsymbol{u}^{(1)} \cdot \left\{(\boldsymbol{u}^{(0)} \cdot \nabla)\boldsymbol{u}^{(0)}\right\}\right\rangle \Big/ \langle u^{(0)} \rangle \tag{37}$$

which is dependent upon the perturbed velocity component but independent of the Reynolds number.

References

[1] C.-M. Ho, Y.-C. Tai, Annu. Rev. Fluid Mech. 30 (1998) 579–612.
[2] P. Tabeling, Introduction a la microfluidique, Belin, Paris, 2003.
[3] E. Lauga, M. Brenner, H. Stone, Handbook of Experimental Fluid Mechanics, Springer, New York, 2007.
[4] R. Pit, H. Hervet, L. Leger, Phys. Rev. Lett. 85 (2000) 980–983.
[5] J.T. Cheng, N. Giordano, Phys. Rev. E 65 (2002) 0312061.
[6] Y. Zhu, S. Granick, Phys. Rev. Lett. 88 (2002) 106102.
[7] E. Bonnacurso, H. Butt, V. Craig, Phys. Rev. Lett. 90 (2003) 1445011.
[8] P. Thompson, S. Troian, Nature 389 (1997) 360–362.
[9] C. Cottin-Bizonne, C. Berentine, E. Charlaix, L. Bocquet, Eur. Phys. J. E 15 (2004) 427–438.
[10] J. Koplik, J.R. Banavar, Annu. Rev. Fluid Mech. 27 (1995) 257.
[11] P. De Gennes, Langmuir 18 (2002) 3413–3414.
[12] J. Ou, B. Perot, J.P. Rothestein, Phys. Fluids 16 (2004) 4635–4643.
[13] J. Ou, J.P. Rothstein, Phys. Fluids 17 (2005) 103606.
[14] K. Watanabe, Y. Udagawa, H. Udagawa, J. Fluid Mech. 381 (1999) 225.
[15] E. Lauga, H. Stone, J. Fluid Mech. 489 (2003) 55.
[16] J. Philip, Z. Angew. Math. Phys. 23 (1972) 353–370.
[17] J. Philip, Z. Angew. Math. Phys. 23 (1972) 960–968.
[18] M. Sbragaglia, A. Prosperetti, J. Fluid Mech. 578 (2007) 435–451.
[19] M. Sbragaglia, A. Prosperetti, Phys. Fluids (2007) (in press). See Physics, 0611042.
[20] H.A. Lorentz, Versl. Kon. Akad. Wet. Amst. 5 (1896) 168.
[21] K. Fukagata, K. Iwamoto, N. Kasagi, Phys. Fluids 18 (2002) L73.
[22] F.H. Harlow, J.E. Welch, Phys. Fluids 8 (1965) 2182–2189.

[23] C. Canuto, M.Y. Hussaini, A. Quarteroni, T.A. Zang, Spectral Methods in Fluid Dynamics, Springer-Verlag, New York, 1988.
[24] T. Kajishima, S. Takiguchi, H. Hamasaki, Y. Miyake, JSME Int. J. Ser. B 44 (2001) 526–535.
[25] S. Succi, The Lattice Boltzmann Equation, Oxford University Press, Oxford, 2001.
[26] D. Wolfe-Gladrow, Lattice Gas Cellular Automata and Lattice Boltzmann Models, Springer, Berlin, 2000.
[27] R. Benzi, S. Succi, M. Vergassola, Phys. Rep. 222 (1992) 145–197.
[28] C. Cercignani, Theory and Application of the Boltzmann Equation, Scottish Academic, New York, 1975.
[29] S. Succi, Phys. Rev. Lett. 89 (2002) 064502.
[30] S. Ansumali, I. Karlin, Phys. Rev. E 66 (2002) 026311.
[31] M. Sbragaglia, S. Succi, Phys. Fluids 17 (2005) 093602.
[32] R. Benzi, L. Biferale, M. Sbragaglia, S. Succi, F. Toschi, J. Fluid Mech. 548 (2006) 257.